Journal Name

COMMUNICATION

Fe_2O_3 nanoparticles-reduced graphene oxide composite for ambient electrocatalytic N_2 reduction to NH_3

Received 00th January 20xx,
Accepted 00th January 20xx

DOI: 10.1039/x0xx00000x

www.rsc.org/

Jian Li,[a] Xiaojuan Zhu,[b,c] Ting Wang,[b,c] Yonglan Luo[c] and Xuping Sun[b*]

Haber-Bosch process for industrial-scale NH_3 production suffers from harsh reaction condtions with CO_2 emission. Electrochemical N_2 reduction has gained considerable recent interest as an eco-friendly and sustainable alternative for NH_3 synthesis with the aid of efficient electrocatalysts for the N_2 reduction reaction (NRR). Here, Fe_2O_3 nanoparticles-reduced graphene oxide composite (Fe_2O_3-rGO) is reported as an earth-abundant NRR electrocatalyst enabling efficient ambient N_2-to-NH_3 conversion. In 0.5 M $LiClO_4$, this Fe_2O_3-rGO attains a large NH_3 yield of 22.13 μg h^{-1} $mg^{-1}_{cat.}$ at –0.50 V and a high Faradaic efficiency of 5.89% at –0.40 V (vs. RHE). It also demonstrates high electrochemical stability.

As an important activated nitrogen feedstock for agricultural fertilizers, NH_3 is key to the growth of the human population and the ecology of the planet.[1] NH_3 has also emerged as an attractive hydrogen energy vector for hydrogen-based economies.[2] As the main current procedure for industrial-scale NH_3 production from atmospheric N_2 and H_2 obtained from fossil fuels, the Haber–Bosch process however operates under harsh reaction conditions, suffering from large energy consumption and heavy serious CO_2 emission.[3]

Electrocatalytic N_2 reduction has received hugh recent research attention as a carbon-neutral process for ambient N_2-to-NH_3 fixation, but it reruires efficient electrocatalysts for the N_2 reduction reaction (NRR) to break the strong N≡N triple bond of inert N_2 and activate the N_2.[4–8] Precious metal-based materials show favorable decent NRR activity,[9–12] but they are too expensive for large-scale uses. As such, great effort has been devloted to designing ande developing earth-abundant alternatives.[13–39] Among such catalyts, transition metal oxides (TMOs) can be easily obtained on a large scale and thus hold greater promise as NRR catalysts. Fe is the only element in all three of the known nitrogenases (MoFe-, VFe-, and FeFe-N_2ase) for biological N_2 fixation,[40] and it also represetns one of the cheapest and most abundant metals on the earth.[41] Licht et al. reported using Fe_2O_3 for efficient N_2 reduction electrocatalysis in a molten hydroxide electrolyte cell at temperatures ≥200 °C.[42] Under ambient conditions, carbon nanotube-supported Fe_2O_3 nanoparticles as a NRR catalyst only achieves a low Faradaic efficiency (FE) of 0.15%.[43] Although much attention has paid on Fe oxides to electrocatalyze the NRR,[16,22, 43–46] it is still highly desired to develop such catalyst system with high performances.

In this communication, we report our recent experimental effort toward this direction in developing Fe_2O_3 nanoparticles-reduced graphene oxide composite (Fe_2O_3-rGO) as a low-cost NRR electrocatalyst which enables efficient ambient N_2 reduction to NH_3 without N_2H_4 by-product. When operated in 0.5 M $LiClO_4$, this Fe_2O_3-rGO composite is able to achieve a large NH_3 yield of 22.13 μg h^{-1} $mg^{-1}_{cat.}$ at –0.50 V vs. reversible hydrogen electrode (RHE) and a high FE of 5.89% at –0.40 V. Notably, it also shows high electrochemical stability.

Fig. 1a shows the X-ray diffraction (XRD) patterns of Fe_2O_3 and Fe_2O_3-rGO (see ESI for preparative details). XRD pattern for Fe_2O_3 gives peaks characteristic of Fe_2O_3 phase (JCPDS No. 79-0007). Fe_2O_3-rGO also shows peaks characteristic of Fe_2O_3 without diffraction peaks for rGO, which could be attributed to its low content. Fig. 1b and 1c show the transmission electron microscopy (TEM) images of rGO and Fe_2O_3-rGO, respectively, suggesting the uniform distribution of nanoparticles (the diameters ranging from 25 to 50 nm) on the surface of rGO. High-resolution TEM (HRTEM) image taken from such nanoparticle reveals well-resolved lattice fringes with an interplanar distance of 0.269 nm corresponding to the (104) plane of Fe_2O_3 (Fig. 1d). The energy-dispersive X-ray (EDX) spectrum (Fig. S1) reveals the existence of Fe, O, and C elements with a weight ratios of 0.52:0.5:0.43 in Fe_2O_3-rGO. STEM and corresponding EDX mapping images (Fig. 1e) confirm the uniform distribution of Fe, O, and C elements within Fe_2O_3-rGO.

[a] *School of Economics and Management, University of Electronic Science and Technology of China, Chengdu 611731, Sichuan, China*

[b] *Institute of Fundamental and Frontier Sciences, University of Electronic Science and Technology of China, Chengdu 610054, Sichuan, China. E-mail: xpsun@uestc.edu.cn*

[c] *Chemical Synthesis and Pollution Control Key Laboratory of Sichuan Province, College of Chemistry and Chemical Engineering, China West Normal University, Nanchong 637002, Sichuan, China*

† *Electronic Supplementary Information (ESI) available: Experimental section and supplementary figures. See DOI:*

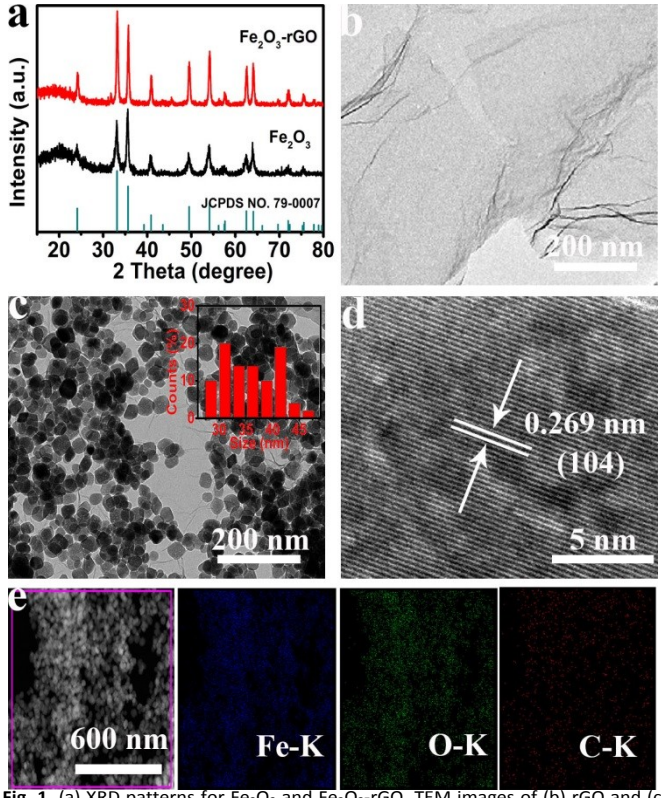

Fig. 1. (a) XRD patterns for Fe_2O_3 and Fe_2O_3-rGO. TEM images of (b) rGO and (c) TiO_2-rGO (inset: the particle size distribution of Fe_2O_3). (d) HRTEM image taken from Fe_2O_3-rGO. (e) STEM and corresponding EDX elemental mapping images of Fe, O, and C elements for Fe_2O_3-rGO.

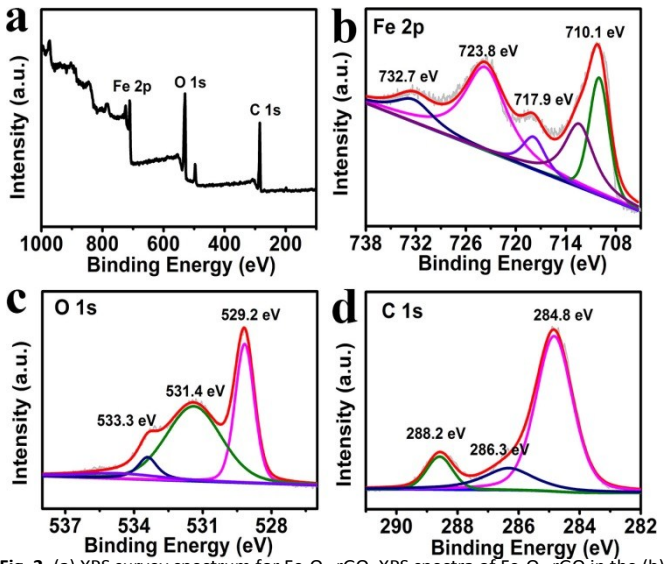

Fig. 2. (a) XPS survey spectrum for Fe_2O_3-rGO. XPS spectra of Fe_2O_3-rGO in the (b) Fe 2p, (c) O 1s, and (d) C 1s regions.

Fig. 2a exhibits the X-ray photoelectron spectroscopy (XPS) survey spectrum of Fe_2O_3-rGO, further indicating the presence of Fe, O, and C elements. XPS spectrum for Fe 2p shown in Fig. 2b exhibits two major peaks with binding energies (BEs) at 710.1 and 723.8 eV, corresponding to Fe $2p_{3/2}$ and Fe $2p_{1/2}$, respectively, which is characteristic of Fe^{3+} in Fe_2O_3.[47,48] Moreover, two shake-up satellites at 717.9 and 732.7 eV are the fingerprint of the electronic structure of Fe_2O_3. In the O 1s region (Fig. 2c), the BEs at 529.2 and 531.4 eV are assigned to O^{2-} and C–O, respectively.[49] In the C 1s region (Fig. 2d), the peak at 284.8 eV reflects the sp^2-hybridized carbon. The peaks at 284.8 and 288.2 eV are attributed to the C–O and carboxylate carbon in O=C–OH, respectively, which are the possible interaction sites between Fe_2O_3/rGO. That is also the main reason why Fe_2O_3 can be well contacted with rGO.[50,51]

Electrochemical measurements of Fe_2O_3-rGO (loaded on carbon paper, Fe_2O_3-rGO/CP loading: 0.2 mg cm^{-2}) were carried out in 0.5 M $LiClO_4$ in an H-shape electrochemical cell. All potentials for NRR were reported on a RHE scale. The concentration of NH_3 and possible N_2H_4 by-product hydrazine were spectrophotometrically determined by the indophenol blue method[52] and Watt and Chrisp, respectively.[53] Fig. S2 and S3 display the corresponding calibration curves. Chronoamperometry experiments were firstly performed for 2h at the potentials ranging from –0.35 to –0.55 V, as shown in Fig. 3a. The produced NH_3 was then measured and related UV-Vis absorption spectra are shown in Fig. 3b.

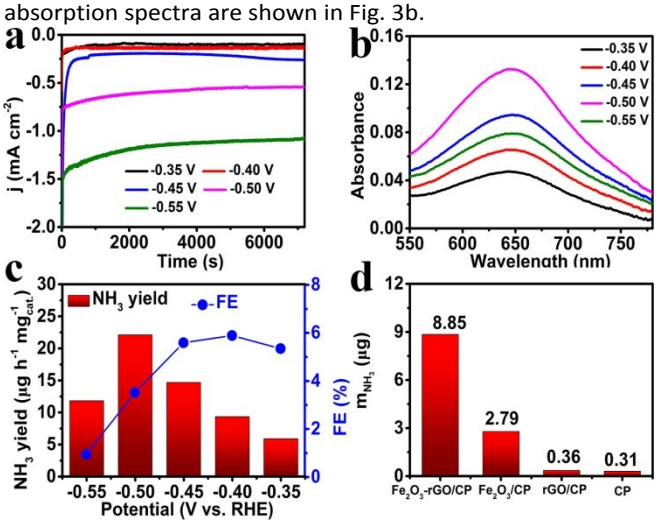

Fig. 3. (a) Time-dependent current density curves for Fe_2O_3-rGO/CP at different potentials in 0.5 M $LiClO_4$. (b) UV–Vis absorption spectra of the electrolytes stained with indophenol indicator at a series of potentials. (c) NH_3 yields and FEs for Fe_2O_3-rGO/CP at different potentials in 0.5 M $LiClO_4$. (d) Amount of NH_3 generated with different electrodes at –0.50 V after 2 h electrolysis.

NH_3 yields and FEs at various potentials are plotted in Fig. 3c. Obviously, Fe_2O_3-rGO/CP achieves the largest NH_3 yield of 22.13 μg h^{-1} $mg^{-1}_{cat.}$ at –0.50 V and the highest FE of 5.89% at –0.40 V, comparing favourably to the behaviours of most Fe-based materials and most other TMOs in aqueous media (Table S1). Moreover, NH_3 yields increases while FEs decrease in the potential ranging of –0.35 V to –0.50 V, which could be attributed to the compromise between increasing current density and competitive selectivity toward hydrogen evolution reaction (HER) rather than NRR. When the applied potential is below –0.50 V, both NH_3 yields and FEs decrease significantly due to the competing hydrogen evolution reaction.[14,28] Note that N_2H_4 was not detected in the electrolytes (Fig. S4), implying Fe_2O_3-rGO/CP has excellent selectivity for NRR. It should be pointed out that rGO/CP and bare CP show poor catalytic activity (Fig. 3d). In sharp contrast, the amount of NH_3 generated for Fe_2O_3-rGO/CP (8.85 μg) is much higher than that of Fe_2O_3/CP (2.79μg). Such superior NRR performance for Fe_2O_3-rGO/CP can be rationally attributed to the following two reasons. (1) Fe_2O_3-rGO has larger surface area (Fig. S5) and thus

exposes more active sites for NRR catalysis;[54] (2) electrochemical impedance spectroscopy data (Fig. S6) show that Fe_2O_3-rGO possesses a lower charge transfer resistance and thus faster NRR kinetics. We also performed electrolysis in 0.1 M $LiClO_4$ at –0.50 V. As shown in Fig. S7, this catalyst performs more efficiently in 0.5 M $LiClO_4$.

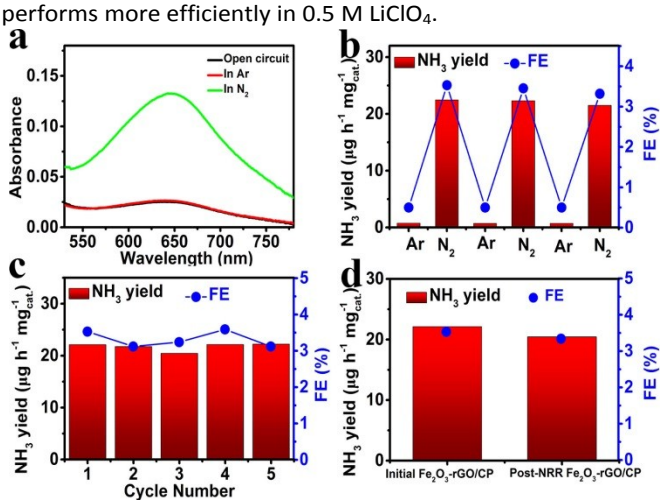

Fig. 4. (a) UV-Vis absorption spectra of the electrolytes stained with indophenol indicator after 2 h electrolysis at –0.50 V under different electrochemical conditions. (b) NH_3 yields and FEs of Fe_2O_3-rGO/CP at –0.50 V with alternating at the interval of 2 h cycles between Ar-saturated and N_2-saturated electrolytes. (c) Recycling test at –0.50 V for Fe_2O_3-rGO/CP. (d) NH_3 yields and FEs at –0.50 V for 2 h over initial Fe_2O_3-rGO/CP and Fe_2O_3-rGO/CP subjected to 24-h operation.

To enture that the detected NH_3 originates from the NRR process by Fe_2O_3-rGO/CP, we performed two control experiments in N_2-saturated solution under open circuit potential and Ar-saturated solution at −0.50 V. In these experiments, only trace NH_3 could be detected by the UV-vis measurements (Fig. 4a). NRR performance of Fe_2O_3-rGO/CP was also tested alternately at –0.50 V in Ar-saturated and N_2-saturated 0.5 M $LiClO_4$. As this result shows, NH_3 is only producted under N_2 atmosphere (Fig. 4b). All data enture that the detected NH_3 originates from the NRR process by Fe_2O_3-rGO/CP. Stability is another critical parameter to evaluate catalyst performance. As shown in Fig. 4c, both NH_3 yields and FEs are well maintained after 5 times of consecutive recycling (Fig. S8). Moreover, 24h electrolysis for Fe_2O_3-rGO/CP at −0.50 V (Fig. S9) shows that the current densities remain almost constant for 24 h. We further determined the NRR performance after 2-h NRR test at –0.50 V in fresh N_2-saturated electrolyte using Fe_2O_3-rGO/CP that has already electrolyzed for 24 h. As shown in Fig. S10 and Fig. 4d, NH_3 yield and FE have negligible change, suggesting Fe_2O_3-rGO/CP has good electrochemical stability for the NRR. In addition, XRD analysis (Fig. S11) demonstrate that such an electrocatalyst is still the Fe_2O_3-rGO in nature after stability test. TEM image (Fig. S12) further shows that Fe_2O_3-rGO keeps its initial morphology after the NRR test.

In summary, Fe_2O_3-rGO composite is reported as an earth-abundant NRR electrocatalyst enabling efficient ambient N_2-to-NH_3 conversion. In 0.5 M $LiClO_4$, Fe_2O_3-rGO/CP achieves a large NH_3 yield of 22.13 μg h^{-1} $mg^{-1}_{cat.}$ at –0.50 V and a high FE of 5.89% at –0.40 V. Notably, it also exhibits excellent selectivity for NH_3 synthesis with good electrochemical stability. This study not only offers us an attractive catalyst material based on earth-abundant elements for ambient electrochemical NH_3 synthesis, but would open up an exciting new avenue to the rational design of graphene-based nanocatalysts for artificial N_2 fixation.

Acknowledgement

This work was supported by the National Natural Science Foundation of China (No. 21575137).

Conflicts of interest

There are no conflicts to declare.

References

1 A. F. Bouwman and K. W. Van Der Hoek, *Atmos. Environ.*, 1997, **31**, 4095–4102.
2 J. N. Renner, L. F. Greenlee, K. E. Ayres and A. M. Herring, *Electrochem. Soc. Interface*, 2015, **24**, 51–57.
3 I. Dybkjaer, *Ammonia Production Processes* (Ed.: A. Nielsen), Springer, Heidelberg, 1995, pp. 199–327.
4 M. A. Shipman and M. D. Symes, *Catal. Today*, 2017, **286**, 57–68.
5 V. Rosca, M. Duca, M. T. de Groot and M. T. M. Koper, *Chem. Rev.*, 2009, **109**, 2209–2244.
6 C. Guo, J. Ran, A. Vasileff and S. Qiao, *Energy Environ. Sci.*, 2018, **11**, 45–56.
7 S. Gao, Y. Zhu, Y. Chen, M. Tian, Y. Yang, T. Jiang and Z. Wang, *Mater. Today*, 2019, DOI: 10.1016/j.mattod.2019.05.004.
8 R. Zhao, H. Xie, L. Chang, X. Zhang, X. Zhu, X. Tong, T. Wang, Y. Luo, P. Wei, Z. Wang and X. Sun, *EnergyChem*, 2019, DOI: 10.1016/j.enchem.2019.100011.
9 M. Shi, D. Bao, B. R. Wulan, Y. Li, Y. Zhang, J. Yan and Q. Jiang, *Adv. Mater.*, 2017, **29**, 1606550.
10 H. Huang, L. Xia, X. Shi, A. M. Asiri and X. Sun, *Chem. Commun.*, 2018, **54**, 11427–11430.
11 J. Wang, L. Yu, L. Hu, G. Chen, H. Xin and X. Feng, *Nat. Commun.*, 2018, **9**, 1795.
12 V. Kordali, G. Kyriacou and C. Lambrou, *Chem. Commun.*, 2000, **17**, 1673–1674.
13 C. Lv, Y. Qian, C. Yan, Y. Ding, Y. Liu, G. Chen and G. Yu, *Angew. Chem., Int. Ed.*, 2018, **57**, 10246–10250.
14 X. Ren, J. Zhao, Q. Wei, Y. Ma, H. Guo, Q. Liu, Y. Wang, G. Cui, A. M. Asiri, B. Li, B. Tang and X. Sun, *ACS Cent. Sci.*, 2019, **5**, 116−121.
15 Z. Wang, F. Gong, L. Zhang, R. Wang, L. Ji, Q. Liu, Y. Luo, H. Guo, Y. Li, P. Gao, X. Shi, B. Li, B. Tang and X. Sun, *Adv. Sci.*, 2018, **5**, 1801182.
16 S. Chen, S. Perathoner, C. Ampelli, C. Mebrahtu, D. Su and G. Centi, *Angew. Chem., Int. Ed.*, 2017, **56**, 2699–2703.
17 J. Zhao, L. Zhang, X.-Y. Xie, X. Li, Y. Ma, Q. Liu, W.-H. Fang, X. Shi, G. Cui and X. Sun, *J. Mater. Chem. A*, 2018, **6**, 24031–24035.
18 H. Cheng, L. Ding, G. Chen, L. Zhang, J. Xue and H. Wang, *Adv. Mater.*, 2018, **30**, 1803694.
19 L. Li, C. Tang, B. Xia, H. Jin, Y. Zheng and S. Qiao, *ACS Catal.*, 2019, **9**, 2902–2908.
20 L. Yang, T. Wu, R. Zhang, H. Zhou, L. Xia, X. Shi, H. Zheng, Y. Zhang and X. Sun, *Nanoscale*, 2019, **11**, 1555–1562.
21 R. Zhang, J. Han, B. Zheng, X. Shi, A. M. Asiri and X. Sun, *Inorg. Chem. Front.*, 2019, **6**, 391–395.
22 J. Kong, A. Lim, C. Yoon, J. H. Jang, H. C. Ham, J. Han, S. Nam, D. Kim, Y. Sung, J. Choi and H. S. Park, *ACS Sustainable Chem. Eng.*, 2017, **5**, 10986–10995.
23 Y. Liu, Y. Su, X. Quan, X. Fan, S. Chen, H. Yu, H. Zhao, Y. Zhang and J. Zhao, *ACS Catal.*, 2018, **8**, 1186−1191.

24 S. Zhang, C. Zhao, Y. Liu, W. Li, J. Wang, G. Wang, Y. Zhang, H. Zhang and H. Zhao, *Chem. Commun.*, 2019, **55**, 2952–2955.
25 Y. Zhang, H. Du, Y. Ma, L. Ji, H. Guo, Z. Tian, H. Chen, H. Huang, G. Cui, A. M. Asiri, F. Qu, L. Chen and X. Sun, *Nano Res.*, 2019, **12**, 919–924.
26 R. Zhang, L. Ji, W. Kong, H. Wang, R. Zhao, H. Chen, T. Li, B. Li, Y. Luo and X. Sun, *Chem. Commun.*, 2019, **55**, 5263–5266.
27 X. Zhu, H. Wang, Z. Liu, R. Zhao, H. Chen, T. Wang, F. Wang, Y. Luo, Y. Wu and X. Sun, *Chem. Commun.*, 2019, **55**, 3987–3990.
28 J. Yu, C. Li, B. Li, X. Zhu, R. Zhang, L. Ji, D. Tang, A. M. Asiri, X. Sun, Q. Li, S. Liu, Y. Luo, *Chem. Commun.*, 2019, **55**, 6401–6404.
29 W. Li, T. Wu, S. Zhang, Y. Liu, C. Zhao, G. Liu, G. Wang, H. Zhang and H. Zhao, *Chem. Commun.*, 2018, **54**, 11188−11191.
30 H. Chen, X. Zhu, H. Huang, H. Wang, T. Wang, R. Zhao, H. Zheng, A. M. Asiri, Y. Luo and X. Sun, *Chem. Commun.*, 2019, **55**, 3152–3155.
31 T. Wang, L. Xia, J. Yang, H. Wang, W. Fang, H. Chen, D. Tang, A. M. Asiri, Y. Luo, G. Cui and X. Sun, *Chem. Commun.*, 2019, **55**, 7502–7505.
32 J. Zhao, B. Wang, Q. Zhou, H. Wang, X. Li, H. Chen, Q. Wei, D. Wu, Y. Luo, J. You, F. Gong and X. Sun, *Chem. Commun.*, 2019, **55**, 4997–5000.
33 W. Guo, Z. Liang, J. Zhao, B. Zhu, K. Cai, R. Zou and Q. Xu, *Small Methods*, 2018, **2**, 1800204.
34 X. Zhang, T. Wu, H. Wang, R. Zhao, H. Chen, T. Wang, P. Wei, Y. Luo, Y. Zhang and X. Sun, *ACS Catal.,* 2019, **9**, 4609–4615.
35 Y. Liu, M. Han, Q. Xiong, S. Zhang, C. Zhao, W. Gong, G. Wang, H. Zhang and H. Zhao, *Adv. Energy Mater.*, 2019, **9**, 1803935.
36 H. Huang, F. Gong, Y. Wang, H. Wang, X. Wu, W. Lu, R. Zhao, H. Chen, X. Shi, A. M. Asiri, T. Li, Q. Liu and X. Sun, *Nano Res.*, 2019, **12**, 1093–1098.
37 X. Li, X. Ren, X. Liu, J. Zhao, X. Sun, Y. Zhang, X. Kuang, T. Yan, Q. Wei and D. Wu, *J. Mater. Chem. A*, 2019, **7**, 2524–2528.
38 X. Li, L. Li, X. Ren, D. Wu, Y. Zhang, H. Ma, X. Sun, B. Du, Q. Wei and B. Li, *Ind. Eng. Chem. Res.*, 2018, **57**, 16622−16627.
39 X. Ren, G. Cui, L. Chen, F. Xie, Q. Wei, Z. Tian and X. Sun, *Chem. Commun.,* 2018, **54**, 8474–8477.
40 T. M. Buscagan, P. H. Oyala and J. C. Peters, *Angew. Chem., Int. Ed.*, 2017, **129**, 7025–7030.
41 P. Jiang, Q. Liu, Y. Liang, J. Tian, A. M. Asiri and X. Sun, *Angew. Chem., Int. Ed.*, 2014, **126**, 13069–13073.
42 S. Licht, B. Cui, B. Wang, F. Li, J. Lau and S. Liu, *Science*, 2014, **345**, 637–640.
43 S. Chen, S. Perathoner, C. Ampelli, C. Mebrahtu, D. Su and G. Centi, *ACS Sustainable Chem. Eng.*, 2017, **5**, 7393–7400.
44 X. Xiang, Z. Wang, X. Shi, M. Fan and X. Sun, *ChemCatChem*, 2018, **10**, 4530–4535.
45 X. Cui, C. Tang, X. Liu, C. Wang, W. Ma and Q. Zhang, *Chem. Eur. J.*, 2018, **24**, 18494–18501.
46 Q. Liu, X. Zhang, B. Zhang, Y. Luo, G. Cui, F. Xie and X. Sun, *Nanoscale*, 2018, **10**, 14386–14389.
47 B. Xu, X. Guan, L. Y. Zhang, X. Liu, Z. Jiao, X. Liu, X. Hu and X. Zhao, *J. Mater. Chem. A*, 2018, **6**, 4048–4054.
48 G. Sun, B. Dong, M. Cao, B. Wei and C. Hu, *Chem. Mater.*, 2011, **23**, 1587–1593.
49 Y. Zhu, S. Cheng, W. Zhou, J. Jia, L. Yang, M. Yao, M. Wang, J. Zhou, P. Wu and M. Liu, *ACS Sustainable Chem. Eng*., 2017, 5, 5067−5074.
50 Z. Shen, H. Xing, Y. Zhu, X. Ji, Z. Liu and L. Wang, *J. Mater. Sci.: Mater. Electron.*, 2017, **28**, 13896–13904.
51 L. Guo, X. Kou, M. Ding, C. Wang, L. Dong, H. Zhang, C. Feng, Y. Sun, Y. Gao and P. Sun, *Sens. Actuators, B*, 2017, **244**, 233–242.
52 D. Zhu, L. Zhang, R. E. Ruther and R. J. Hamers, *Nat. Mater.*, 2013, **12**, 836–841.
53 G. W. Watt and J. D. Chrisp, *Anal. Chem.*, 1952, **24**, 2006–2008.
54 J. Zhao, X. Ren, X. Li, D. Fan, X. Sun, H. Ma, Q. Wei and D. Wu, *Nanoscale*, 2019, **11**, 4231–4235.

